Macro-Fiber Composite Actuated Piezoelectric Robotic Fish

Alper Erturk

Abstract This chapter is centered on fish-like aquatic robotics using flexible bimorphs made from Macro-Fiber Composite (MFC) piezoelectric laminates. Bimorph propulsors employing MFCs offer a balance between the actuation force and velocity response for performance enhancement in bio-inspired swimming, in addition to noiseless and efficient actuation over a range of frequencies, geometric scalability, and simple design. The experimental component of this work first explores the effect of a passive substrate fin extension on the thrust frequency response of MFCs bimorphs in quiescent water along with measurement procedures. Specifically, it is shown that broadband thrust generation can be achieved in the presence of a passive substrate extension. The second part of the experiments is focused on the characterization of an elastically constrained uniform MFC bimorph propulsor (in-air and underwater) as well as the development of a robotic fish prototype combining a microcontroller and a printed circuit board amplifier to generate high actuation voltage for untethered locomotion. A distributed-parameter electroelastic model including the hydrodynamic effects and actuator dynamics is coupled with the elongated-body theory for estimating the mean thrust in quiescent water. For electroelastically nonlinear actuation levels, experimentally obtained underwater vibration response is coupled with the elongated-body theory to predict the thrust output. The measured mean thrust levels in quiescent water (on the order of ~ 10 mN) compare favorably with thrust levels of biological fish. An untethered robotic fish prototype that employs a single bimorph fin for straight swimming and turning motions is developed and tested in free locomotion. A swimming speed of 0.3 body length/s (7.5 cm/s swimming speed for 24.3 cm body length) is reported at 5 Hz for a nonoptimized main body-propulsor bimorph combination under a moderate actuation voltage level.

A. Erturk (✉)
G.W. Woodruff School of Mechanical Engineering, Georgia Institute of Technology, Atlanta, GA 30332, USA
e-mail: alper.erturk@me.gatech.edu

R. Du et al. (eds.), *Robot Fish*, Springer Tracts in Mechanical Engineering,
DOI 10.1007/978-3-662-46870-8_9

1 Introduction

The potential applications for fish-like biomimetic locomotion at different geometric scales range from underwater sensing and exploration for sustainable ecology to drug delivery and disease screening in medicine [1–3]. Other than the use of conventional actuators, such as servomotors and hydraulic actuators employed in conjunction with various mechanisms [4–13], recently, various smart materials have been utilized for fish-like robotic fish development, such as Ionic Polymer-Metal Composites (IPMCs) [14–31], Shape Memory Alloys (SMAs) [32–37], and magnetostrictive thin films [38–40], among other alternatives [41–43]. In particular, the IPMC technology [14–31] has received great interest for biomimetic locomotion primarily due to its low-voltage actuation and large amplitude deflection capabilities. Conventional motor-based actuation involves complex structural design and provides high swimming speeds (per body length); whereas, the use of smart materials enables the geometric scalability option along with simple design and noiseless performance at the expense of reduced swimming speeds.

Piezoelectric materials offer strong electromechanical coupling and actuation forces, high power density, and their fabrication methods at different scales are well established [44–47]. These materials exhibit the so-called direct and converse piezoelectric effects. The direct effect is the process of electric charge development in response to mechanical deformation, while the converse effect is the mechanical deformation resulting from an applied electric field in a piezoelectric material. From the standpoint of multifunctionality, the converse piezoelectric effect can be used for dynamic actuation in biomimetic locomotion over a range of frequencies, while the direct piezoelectric effect can be employed for harvesting underwater energy toward enabling self-powered swimmer-sensor platforms [46]. Similar to IPMCs, the Macro-Fiber Composite (MFC) piezoelectric actuators (introduced by the NASA Langley Research Center in the first decade of this century [48–51]) also exhibit high efficiency in size, reduced energy consumption, and noiseless performance. In addition, unlike IPMCs, the MFCs offer large dynamic stresses in bending actuation as well as high performance for both low-frequency and high-frequency applications. The MFC technology employs piezoelectric (PZT: lead zirconate titanate) fibers of rectangular cross-section in epoxy matrix along with interdigitated electrodes and it leverages the 33-mode of piezoelectricity in bending actuation, i.e., strain and electric field directions are coincident (Fig. 1). The composite architecture is embedded in Kapton film which provides substantial structural robustness and integrity. Furthermore, polyester electrode sheets enable the option of waterproof applications. With these characteristics, MFC-based robotic fish can provide both geometric scalability and high performance swimming, as discussed in detail throughout this chapter.

High-voltage input requirement and low-strain output are the two downsides of piezoelectric transduction limiting the application of previously investigated piezoelectric structures for robotic fish development to use in free locomotion. In order to overcome the shortage of low strain in piezoelectric robotic configurations prior

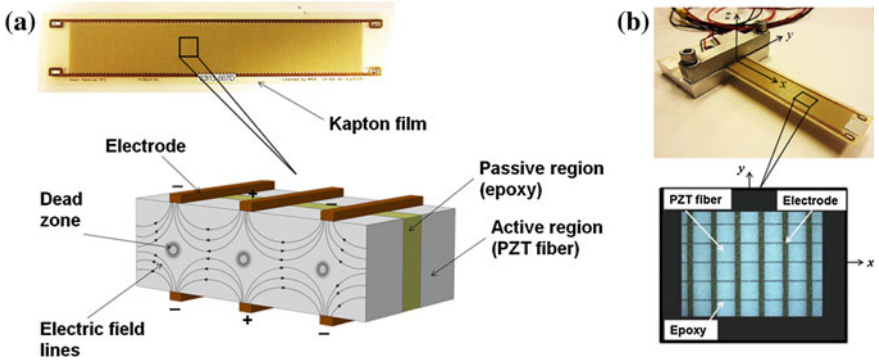

Fig. 1 **a** Picture of a single MFC laminate and close-up schematic of the piezoelectric fibers, epoxy matrix, and interdigitated electrodes; **b** picture of a bimorph cantilever made from two MFC laminates (bonded in a vacuum process using high shear strength epoxy) for bending actuation and close-up view of a small region showing the major components of the composite electromechanical structure

to the MFC technology, various kinematic magnification mechanisms were proposed by others [52–54]. However, the magnification component that is employed for creating larger vibration amplitudes typically creates energy loss and noise. As far as the high-input voltage requirement is concerned, research groups have used tethered configurations to power piezoelectric robotic fish, which restricts the free (unconstrained) locomotion capability [52–55]. Only recently, an untethered piezoelectric robotic fish [56] was reported by using an MFC bimorph as the propulsor with simple electronics and no motion amplification mechanism.

In this chapter, fish-like aquatic robotics using MFC piezoelectric bimorphs is presented based on our recent work [46, 56]. Focusing on quiescent water condition, extensive experiments are conducted to measure the thrust generated by MFCs oscillated under resonant actuation. Performance comparison of two MFC fish configurations with and without as passive caudal fin extension is presented by reviewing the work by Erturk and Delporte [46] in detail. In-air and underwater dynamics of an MFC bimorph cantilever are modeled for linear bending vibrations under dynamic piezoelectric actuation. The in-air electroelastic model is extended to obtain an underwater electrohydroelastic model accounting for the hydrodynamic effects. Underwater dynamics of an elastically constrained bimorph propulsor is then coupled with Lighthill's elongated-body theory to predict the thrust output in quiescent water based on Lighthill's mean thrust expression. In-air and underwater experiments are conducted for model validation and for characterizing a bimorph propulsor. Finally, an untethered robotic fish prototype is reported for straight swimming and turning motions in free locomotion based on the work by Cen and Erturk [56].

2 Underwater Thrust Generation Using MFCs and Effect of a Passive Fin Extension

2.1 Calibration of the Thrust Measurement Setup

Hydrodynamic thrust measurement under piezoelectric actuation is a more involved task as compared to measurements of the dynamic kinematic variables, such as velocity and acceleration. The reason is that the thrust output is a one-directional force resultant achieved during the oscillatory actuation of the piezoelastic structure at steady state. A 254 mm × 25.4 mm × 6.35 mm aluminum cantilever is combined with a laser sensor to obtain an elastic transducer for this purpose. The MFC fish sample with its plexiglass clamp is attached to the tip of the horizontally located *transducer cantilever* as shown in Fig. 2a. A set of small masses are then gradually located at the center of the MFC fish head to emulate the force (thrust) by the help of the gravity. The resulting deflection is recorded by the laser sensor (Fig. 2b) and eventually the linear calibration curve shown in Fig. 2c is obtained. Note that the transducer cantilever responds linearly up to several hundreds of milli-Newtons and the decoder of the laser sensor is sensitive enough to capture the resulting deflection amplitudes.

2.2 Underwater Actuation and Thrust Measurement

After the calibration curve of the transducer cantilever is obtained in air, the transducer cantilever with a clamped MFC fish sample is immersed in water for the hydrodynamic thrust measurements using the experimental setup shown in Fig. 3a. It is important to note that the dimensions of the transducer cantilever are such that its underwater fundamental resonance frequency is sufficiently higher than the underwater actuation frequencies of interest (this is checked by impact hammer

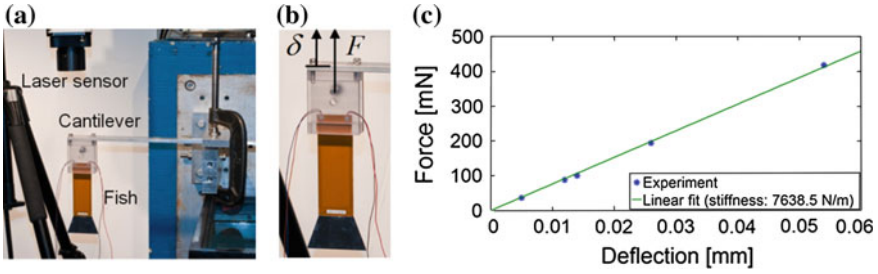

Fig. 2 **a** Calibration of the setup to obtain the force-deflection relationship in the presence of an MFC fish sample and its clamp; **b** close-up view showing the point of applied calibration loads (F) at the head of the MFC fish and the point of deflection (δ) measurement; **c** linear calibration curve with the identified linear stiffness (F/δ) value (© IOP Publishing. Reproduced with permission. All rights reserved)

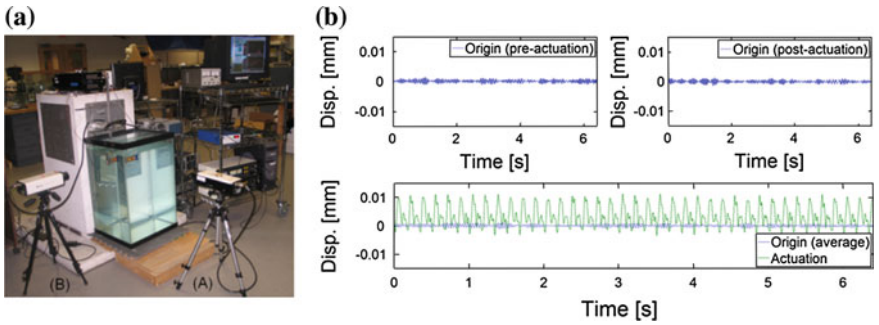

Fig. 3 **a** Experimental setup used for underwater thrust measurement after the transducer cantilever with a clamped MFC fish sample is submerged in water. Laser A is used for obtaining the transverse tail velocity-to-actuation voltage input FRFs whereas Laser B is used to measure the mean head displacement during the manual frequency sweep for evaluating the hydrodynamic thrust; **b** displacement measurements at the head of the MFC fish sample (in the direction of positive thrust) during pre-actuation, post-actuation, and actuation (along with the average of the pre-actuation and post-actuation histories, which defines the averaged origin) (© IOP Publishing. Reproduced with permission. All rights reserved)

testing). Hence, the measurement is in the quasi-static region of the transducer cantilever in the thrust generation experiments and the tip deflection of the cantilever is due to the dynamics of the MFC fish sample only (i.e., there is no interaction with the dynamics of the transducer cantilever). In addition, the hydrostatic pressure distributions on both faces of the transducer cantilever cancel each other so that the in-air thrust-deflection calibration is valid.

In Fig. 3a, the laser vibrometer pointing from the transverse direction of the MFC fish sample (Laser A) is employed for extracting the modal frequencies of the MFC fish sample (in bending) through the tail velocity-to-actuation voltage FRFs. The second laser vibrometer (Laser B) measures the displacement of the transducer cantilever (as in Fig. 2a) in the perpendicular direction so that the mean displacement can be converted to thrust using the calibration curve (Fig. 2c).

Harmonic actuation is used for hydrodynamic thrust generation. The frequency increment used in the time-domain thrust measurements is 0.5 Hz. At each frequency of voltage actuation, three time-domain displacement measurements are taken (using Laser B in the configuration described by Fig. 3a): Pre-actuation, actuation, and post-actuation. An example is displayed in Fig. 3b for the thrust measurement at 6 Hz under the peak-to-peak actuation input of 1050 V. The first measurement in this scheme is the *pre-actuation* measurement, which is simply the laser reading in the absence of piezoelectric actuation (i.e., noise around the origin). Then, the voltage actuation is started and the data is recorded after the system reaches its steady state, which is the *actuation* measurement. Finally, the actuation is stopped and a last measurement is taken in the absence of any actuation or transients. This is the *post-actuation* measurement. The origin is defined as the average of the pre-actuation and post-actuation measurements. The mean displacement caused by the thrust is the difference between the mean value of the

actuation measurement and the mean value of the averaged origin measurement. The mean displacement reading is then used in Fig. 2c to give the mean thrust at the frequency of measurement. Note that the laser signal amplitude is divided by the refractive index of water ($n = 1.333$) in the underwater experiments and the validity of this signal correction is checked through another set of experiments not discussed here. Another important optical consideration when taking laser measurements through a transparent but reflective interface (clean glass in this case) is to make sure that the reflection from the interface is *not* on the lens.

2.3 The Effect of a Passive Caudal Fin Extension on the Thrust Frequency Response

Two bimorph fish samples are fabricated using a 0.127-mm-thick aluminum sheet as the substrate material and MFC piezoelectrics as the active material (MFC-8528-P1 type from the Smart Material Corporation). The active length and width of the MFC layers are 85 and 28 mm, respectively. The MFC layers are bonded onto both faces of the aluminum substructure using high-shear-strength epoxy in a vacuum bonding process. The active region of each bimorph MFC fish is approximately 0.8-mm thick. As shown in Fig. 4, one of the two MFC fish configurations has no caudal fin; whereas, the aluminum substrate of the other bimorph extends outside the active region to give a passive tapered caudal fin of 35 mm length and 48 mm maximum width (at the tail tip). Each MFC layer has a free capacitance of 5.7 nF according to the manufacturer and parallel connection is employed here. Therefore, a resultant capacitance of 11.4 nF is expected for each unclamped MFC fish sample based on the technical specifications. The measured clamped capacitance values (in-air) are 7.4 and 8.6 nF for the configurations without and with a caudal fin, respectively.

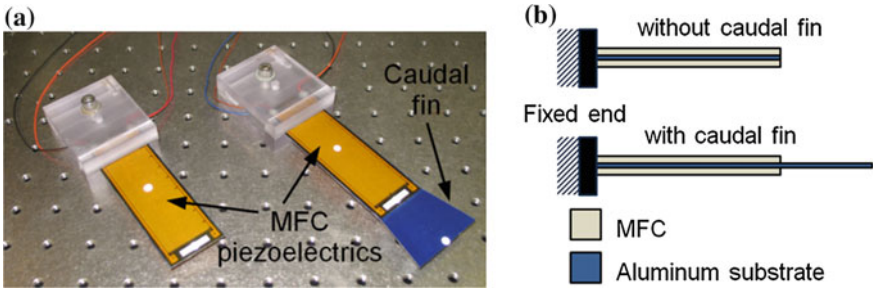

Fig. 4 **a** Bimorph MFC fish samples without and with a passive caudal fin and **b** side-view schematics of the composite bimorph structures (not to scale). Both samples have continuous aluminum substrates (*blue*) of the same thickness but different length (© IOP Publishing. Reproduced with permission. All rights reserved)

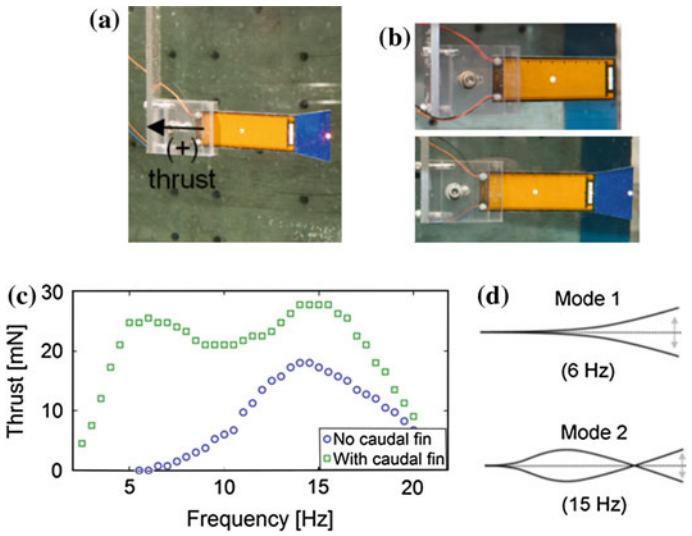

Fig. 5 **a** Underwater configuration of an MFC fish sample; **b** two MFC fish configurations without and with a passive caudal fin; **c** comparison of thrust frequency response for the same actuation input (peak-to-peak voltage: 1050 V) showing the substantial advantage of the MFC fish sample with a caudal fin; **d** mode shapes of the configuration with a passive caudal fin (© IOP Publishing. Reproduced with permission. All rights reserved)

The MFC fish samples are attached to the transducer cantilever for the underwater thrust measurements. Figure 5a shows the alignment of the transducer cantilever with a bimorph MFC fish sample attached at its tip. The underwater configurations of the two MFC fish samples without and with a caudal fin are shown in Fig. 5b. The thrust measurements are conducted for frequencies below 20 Hz (which cover the first two bending modes of the MFC fish sample with a passive caudal fin). For the same harmonic actuation voltage input to each sample (1050 V of peak-to-peak voltage), Fig. 5c shows the thrust FRFs. The fundamental resonance frequency of the MFC fish sample with no caudal fin is around 14.5 Hz and the mean thrust at this frequency is 18 mN. Remarkably, the MFC fish sample with a tapered passive caudal fin exhibits two peaks in the frequency range of 0–20 Hz with much larger thrust output. In addition to its fundamental vibration mode around 6 Hz (the first bending mode), the MFC fish with a passive caudal fin has its second vibration mode around 15 Hz (the second bending mode). The mean thrust readings for the sample with a passive caudal fin in Fig. 5c are 26 mN at 6 Hz (mode 1) and 28 mN at 15 Hz (mode 2). The mode shapes of this configuration are shown in Fig. 5d. Note that the second mode shape (at 15 Hz) has a node near the root of the caudal fin, hence an inflection point close to the head of the MFC fish. It can be concluded from Fig. 5c that the configuration with a passive caudal fin is a *wideband thrust generator* with substantially larger and relatively flat thrust output as compared to the configuration with no caudal fin for the same dynamic actuation input.

It is worth mentioning that the actuation performance for the second vibration mode can be improved by optimizing the surface coverage of the piezoelectric layers. It is known that the second mode shape (in Fig. 5d) has a *strain node* (which is simply an inflection point for a thin cantilever) near the root. Therefore, a significant portion of the actuation input cancels itself with the present surface coverage of the piezoelectric layers since the strain distributions on two sides of the strain node are 180° out of phase. Using segmented piezoelectrics (or segmented electrodes) can improve actuation performance dramatically for swimming with the second mode shape.

2.4 The Effect of Actuation Voltage on the Thrust Output

Further experiments are conducted with both MFC fish samples to investigate the dependence of the thrust output on the actuation voltage. The allowable voltage range of the MFC actuators is −500 to 1500 V and neither of these levels should be exceeded during the dynamic actuation. Therefore, the maximum peak-to-peak voltage input level without imposing any DC offset is 1000 V and this level can be increased up to the peak-to-peak level of 2000 V with sufficient DC offset (i.e., using +500 V DC offset with an oscillatory amplitude of 1000 V so that the maximum is 1500 V and the minimum is −500 V). In this work, the peak-to-peak voltage levels of 800, 1050, and 1300 V are studied and the resulting thrust frequency response curves are shown in Fig. 6. The thrust output increases monotonically with increasing voltage amplitude at every frequency. For all peak-to-peak actuation voltage levels shown in Fig. 6, the configuration with a passive caudal fin results in substantially better thrust generation performance with larger peak thrust as well as wideband behavior. At the highest actuation voltage level (1300 V peak-to-peak), mean thrust values of more than 30 mN are achieved over the frequency range of 4–17 Hz (with the peak values of 40 and 50 mN at the first two resonance frequencies, respectively). Note that the mass of the configuration with a passive caudal fin is only 10 g (excluding the mass of its plexiglass clamp head).

3 Piezohydroelastic Modeling of a Uniform MFC Propulsor Dynamics

3.1 In-Air Dynamics of a Bimorph Propulsor

The linear electroelastic equation of motion for in-air bending vibrations of a thin bimorph cantilever (Fig. 7) with uniform cross-section under dynamic voltage actuation is given by

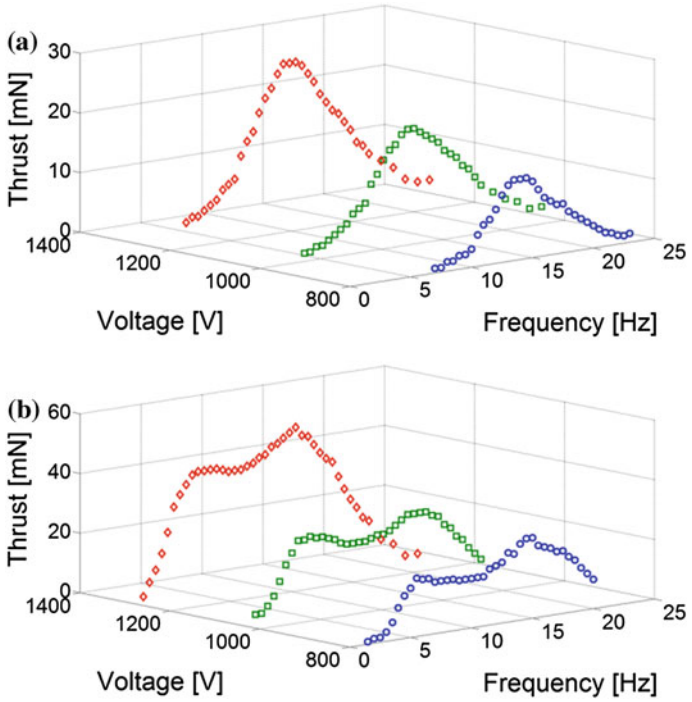

Fig. 6 Mean thrust frequency response curves of different peak-to-peak actuation voltage levels for the configurations **a** without and **b** with a passive caudal fin (© IOP Publishing. Reproduced with permission. All rights reserved)

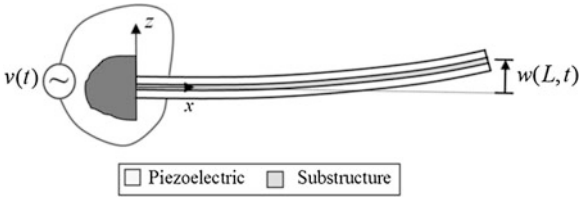

Fig. 7 Schematic of a uniform cantilevered bimorph propulsor under dynamic voltage actuation to create bending vibrations (piezoelectric layers can be combined in series or in parallel) (© IOP Publishing. Reproduced with permission. All rights reserved)

$$D\frac{\partial^4 w(x,t)}{\partial x^4} + m\frac{\partial^2 w(x,t)}{\partial t^2} + c\frac{\partial w(x,t)}{\partial t} = \vartheta\left[\frac{\mathrm{d}\delta(x)}{\mathrm{d}x} - \frac{\mathrm{d}\delta(x-L)}{\mathrm{d}x}\right]v(t) \qquad (1)$$

where D is the flexural rigidity of the composite cross-section, m is the mass per length, c is the damping coefficient, ϑ is the electromechanical coupling term in the physical coordinates, $\delta(x)$ is the Dirac delta function, $v(t)$ is the actuation voltage, and $w(x,t)$ is the deflection of the reference surface in the transverse (z) direction at

the longitudinal position x and time t. Here, m and c are altered for underwater vibrations due to the added mass and damping effects of hydrodynamic loads as discussed in Sect. 3.2. While the formulation is given for a uniform cross-section (e.g., the case of no caudal fin extension in the previous section), a similar modeling approach can easily be used in the case of a two-segment configuration with a substrate extension as long as the individual segments are uniform.

Separating the space- and time-domain variables and assuming single-mode (fundamental mode) response yields

$$w(x,t) \cong \phi(x)\eta(t) \tag{2}$$

where $\phi(x)$ and $\eta(t)$ are the mass-normalized eigenfunction and the modal coordinate of the fundamental transverse vibration mode for a clamped-free uniform beam. The mass-normalized eigenfunction for the first mode can be obtained as

$$\phi(x) = \sqrt{\frac{1}{mL}}\left[\cosh\frac{\lambda x}{L} - \cos\frac{\lambda x}{L} - \sigma\left(\sinh\frac{\lambda x}{L} - \sin\frac{\lambda x}{L}\right)\right] \tag{3}$$

and it satisfies

$$\int_0^L m\phi^2(x)\mathrm{d}x = 1, \quad \int_0^L \phi(x) D\frac{\mathrm{d}^4\phi(x)}{\mathrm{d}x^4}\mathrm{d}x = \omega_{n,\mathrm{air}}^2 \tag{4}$$

Here, $\lambda = 1.87510407$, $\sigma = 0.734095514$, L is the length of the bimorph, and $\omega_{n,\mathrm{air}}$ is the in-air natural frequency:

$$\omega_{n,\mathrm{air}} = \lambda^2\sqrt{\frac{D}{m_s L^4}} \tag{5}$$

where m_s is the structural mass per length.

For in-air vibrations, the mass per length in Eq. (1) is merely the structural mass per length:

$$m = m_s \tag{6}$$

while the in-air damping coefficient is

$$c = 2m_s\zeta_s\omega_{n,\mathrm{air}} \tag{7}$$

where ζ_s is the damping ratio which is assumed to be dominated by structural losses for infinitesimal in-air vibrations.

Following the standard analytical modal analysis procedure [57], i.e., substituting Eq. (2) into Eq. (1), multiplying the latter by the eigenfunction and integrating the resulting equation over the beam length, one obtains

$$\begin{aligned}\frac{\mathrm{d}^2\eta(t)}{\mathrm{d}t^2}\int_0^L m\phi^2(x)\mathrm{d}x+\frac{\mathrm{d}\eta(t)}{\mathrm{d}t}\int_0^L c\phi^2(x)\mathrm{d}x+\eta(t)\int_0^L \phi(x)D\frac{\mathrm{d}^4\phi(x)}{\mathrm{d}x^4}\mathrm{d}x\\ =v(t)\int_0^L \phi(x)\vartheta\left[\frac{\mathrm{d}\delta(x)}{\mathrm{d}x}-\frac{\mathrm{d}\delta(x-L)}{\mathrm{d}x}\right]\mathrm{d}x\end{aligned} \tag{8}$$

yielding

$$\frac{\mathrm{d}^2\eta(t)}{\mathrm{d}t^2}+2\zeta_s\omega_{n,\mathrm{air}}\frac{\mathrm{d}\eta(t)}{\mathrm{d}t}+\omega_{n,\mathrm{air}}^2\eta(t)=\theta v(t) \tag{9}$$

where θ is the electromechanical coupling term in the generalized modal coordinate η:

$$\theta=\int_0^L \phi(x)\vartheta\left[\frac{\mathrm{d}\delta(x)}{\mathrm{d}x}-\frac{\mathrm{d}\delta(x-L)}{\mathrm{d}x}\right]\mathrm{d}x=\vartheta\frac{\mathrm{d}\phi(x)}{\mathrm{d}x}\bigg|_{x=L} \tag{10}$$

If the actuation voltage is assumed to be harmonic of the form

$$v(t)=V_0e^{j\omega t} \tag{11}$$

where V_0 is the actuation voltage amplitude, ω is the actuation frequency (in rad/s), and j is the unit imaginary number, then the steady-state response for the modal coordinate is

$$\eta(t)=\frac{\theta V_0e^{j\omega t}}{\omega_{n,\mathrm{air}}^2-\omega^2+j2\zeta_s\omega_{n,\mathrm{air}}\omega} \tag{12}$$

The resulting in-air tip velocity amplitude is therefore

$$\left|\frac{\partial w(L,t)}{\partial t}\right|\cong\left|\phi(L)\frac{\mathrm{d}\eta(t)}{\mathrm{d}t}\right|=\left|\frac{V_0\omega\theta\phi(L)}{\omega_{n,\mathrm{air}}^2-\omega^2+j2\zeta_s\omega_{n,\mathrm{air}}\omega}\right| \tag{13}$$

from which the tip velocity-to-actuation voltage frequency response function (FRF) can be extracted. It is important to note that this solution is valid for excitations around the fundamental natural frequency since higher vibration modes are not used in Eq. (2). In addition, the foregoing derivation neglects the geometric, material, and dissipative nonlinearities [58–60] and is strictly valid for linear vibrations only.

3.2 Underwater Dynamics of a Bimorph Propulsor

Hydrodynamic effects are included to predict the underwater vibrations of the cantilever based on the previous work by Sader and coworkers [61–63] on atomic force microscopy cantilevers as a straightforward approach for slender configurations. Similar efforts are due to Brunetto et al. [23], Mbemmo et al. [24], and Aureli et al. [28] for the underwater dynamics of IPMC propulsors. The following hydroelastic formulation [61–63] assumes geometrically small oscillations (relative to both length and width dimensions) of a uniform cantilever in unbounded fluid. Moreover, Sader's theory [61–63] assumes that the length-to-width ratio (L/b) is large and the accuracy of predictions decay as L and b become comparable [64] due to nonlinear 3-D hydrodynamic effects.

The added mass per length m_a and the hydrodynamic damping ratio ζ_h can be expressed in terms of the hydrodynamic function Γ as [61]

$$m_a = \frac{\pi \rho_w b^2}{4} \Gamma_r \tag{14}$$

$$\zeta_h = \frac{1}{2Q_h} = \frac{\Gamma_i}{2\left(\frac{4m_s}{\pi \rho_w b^2} + \Gamma_r\right)} \tag{15}$$

where ρ_w is the mass density of water, Q_h is the quality factor due to hydrodynamic damping, Γ_r, and Γ_i are the real and imaginary parts of hydrodynamic function Γ, respectively, and b is the width of the bimorph propulsor. The hydrodynamic function Γ can be calculated analytically or numerically. Simplified expressions of the hydrodynamic function Γ are available depending on the range of the Reynolds number [65, 66]. Although the present discussion is given for small oscillations, we note that particularly hydroelastic nonlinearities can easily be pronounced due to large amplitude vibrations and for comparable aspect ratios, requiring correction of the hydrodynamic function [64, 66].

As far as the dissipation mechanisms are concerned, both structural and hydrodynamic damping effects are taken into account for the total damping ratio (ζ_w) of underwater vibrations:

$$\zeta_w = \zeta_s + \zeta_h \tag{16}$$

The mass per length and damping coefficient terms in Eq. (1) for underwater vibrations are

$$m = m_w = m_s + m_a \tag{17}$$

$$c = 2m\zeta_w \omega_{n,\text{water}} = 2m_w(\zeta_s + \zeta_h)\omega_{n,\text{water}} \tag{18}$$

and the mass-normalized eigenfunction in Eq. (2) satisfies

$$\int_0^L m\phi^2(x)\mathrm{d}x = 1,\ \int_0^L \phi(x)D\frac{\mathrm{d}^4\phi(x)}{\mathrm{d}x^4}\mathrm{d}x = \omega_{n,\text{water}}^2 \tag{19}$$

Since the underwater mass per length is due to Eq. (17), the underwater natural frequency $\omega_{n,\text{water}}$ is obtained from the in-air natural frequency $\omega_{n,\text{air}}$ (which is approximately the in-air resonance frequency for $\zeta_s \ll 1$) through Chu's formula [67] (for large aspect ratio) modified by the real part of the hydrodynamic function Γ_r [61]:

$$\omega_{n,\text{water}} = \omega_{n,\text{air}}\sqrt{\left(1+\frac{\pi\rho_w b^2}{4m_s}\Gamma_r\right)^{-1}} \tag{20}$$

where $\omega_{n,\text{air}}$ is given by Eq. (5).

The resulting underwater tip velocity response amplitude is therefore

$$\left|\frac{\partial w(L,t)}{\partial t}\right| \cong \left|\phi(L)\frac{\mathrm{d}\eta(t)}{\mathrm{d}t}\right| = \left|\frac{V_0\omega\theta\phi(L)}{\omega_{n,\text{water}}^2 - \omega^2 + j2\zeta_w\omega_{n,\text{water}}\omega}\right| \tag{21}$$

where θ is due to Eq. (10). However, the eigenfuction $\phi(x)$ in Eqs. (10) and (21) is now normalized according to Eq. (19) with m given by Eq. (17), i.e., the mass term in Eq. (3) is due to Eq. (17) for underwater vibrations.

3.3 Hydrodynamic Mean Thrust in Terms of the Underwater Velocity Response

In most cases of robotic fish thrust estimation [27, 28, 38–40], it becomes necessary to identify certain calibration factors, such as the drag coefficient, which removes the possibility of obtaining an a priori estimate of the thrust resultant solely from the underwater vibration response. Lighthill's elongated-body theory was used in previous IPMC-based robotic fish studies to predict the steady-state cruising speed [24, 27] by equating the thrust expressions from the reactive and resistive methods, where the drag coefficient was measured by spring scales while pulling the fish with different velocities. In the present work, Lighthill's theory [68–71] is employed alone to estimate the mean thrust in quiescent water as a first approximation. The mean thrust (T) in Lighthill's theory is given in the presence of an external relative free stream of speed U (which is essentially the swimming speed) as

$$T = \frac{1}{2}m_v\left[\overline{\left(\frac{\partial w}{\partial t}\right)^2} - U^2\overline{\left(\frac{\partial w}{\partial x}\right)^2}\right]_{x=L} \tag{22}$$

where the over-bar stands for the mean value and m_v is the virtual mass density at $x = L$, expressed as

$$m_v = \frac{\pi \rho_w b^2}{4} \beta \tag{23}$$

Here, β is a virtual mass coefficient that is close to unity [70] for the wavelength and body length considered in this work (hence $\beta \cong 1$) with slender body assumption. Once again, aspect ratio effects can alter this term as well [64, 66] due to hydrodynamic nonlinearities which can be accounted for (by an aspect ratio-dependent inertia coefficient as in well-known semi-empirical Morison's equation).

In Eq. (22), we set $U \to 0$ to approximate quiescent water condition:

$$T \cong \frac{1}{2} m_v \overline{\left(\frac{\partial w}{\partial t} \right)^2} \Bigg|_{x=L} = \frac{\pi \rho_w b^2}{8} \overline{\left(\frac{\partial w(L,t)}{\partial t} \right)^2} \tag{24}$$

where the mean thrust T depends only on the tip velocity and the virtual mass for quiescent water approximation.

4 Details of the Experimental Setup for Model Validation

4.1 Setup for In-Air Tip Velocity FRF Measurements

The MFC bimorph tested and characterized in the experiments is shown in Fig. 8 along with its clamp and fixture employed for the in-air actuation FRF measurements. The bimorph is made of two custom-made hydrophobic M8528-P1 [51] MFC laminates with no separate substructure layer other than the Kapton and epoxy layers of the MFCs. A vacuum bonding process is employed by using high shear strength epoxy to assemble the piezoelectric laminates (this process is described

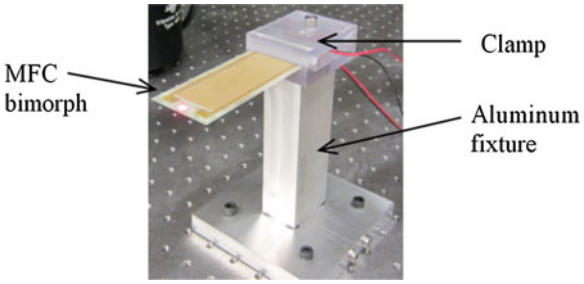

Fig. 8 In-air configuration of the bimorph MFC cantilever for the measurement of its tip velocity-to-actuation voltage FRF (© IOP Publishing. Reproduced with permission. All rights reserved)

elsewhere [72]). The electrode leads of the two MFCs are combined in parallel throughout the experiments discussed in this chapter. A vertically aligned laser vibrometer is used along with the monitored actuation signal in order to obtain the transverse (vertical direction in Fig. 8) tip velocity-to-actuation voltage FRFs of the MFC bimorph in air.

4.2 Setup for Underwater Tip Velocity FRF and Mean Thrust Measurements

The experimental setup used for the underwater tip velocity and thrust measurements is shown in Fig. 9a. As shown in Fig. 9b, the MFC bimorph is fixed with the same clamp in the underwater experiments. Laser (1) measures the transverse tip velocity under dynamic actuation while Laser (2) provides the head displacement (constrained by an aluminum cantilever) through a small mirror that makes a 45° angle with the horizontal plane. The elastically constrained mean head displacement is correlated to the mean thrust as described in the next section. Note that both laser signals (velocity and displacement) are divided by the refractive index of water in the underwater experiments [46] as discussed in Sect. 2.1 (note that the setup and the calibration cantilever are different from those reviewed in more detail in Sect. 2; however, the basic measurement concept is the same).

4.3 Calibration of the Thrust Measurement Setup

The MFC bimorph and its clamp are fixed at the tip of a horizontally located aluminum beam which functions as a *transducer cantilever* along with a vertically pointing laser vibrometer used in the displacement measurement mode (Fig. 10a).

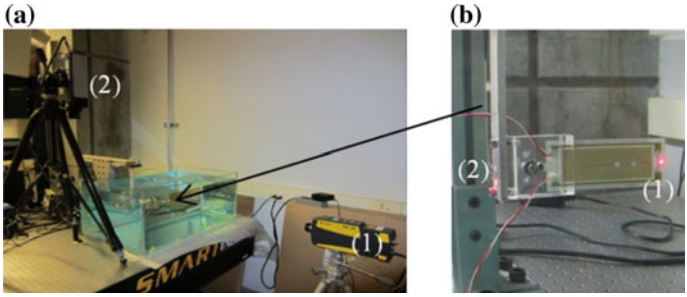

Fig. 9 **a** Experimental setup used for thrust measurement of a bimorph propulsor in quiescent water: Laser *(1)* measures the transverse tip velocity while Laser *(2)* measures the elastically constrained head displacement through a 45° mirror; **b** close-up view showing the measurement points of Lasers *(1)* and *(2)* on the MFC bimorph propulsor (© IOP Publishing. Reproduced with permission. All rights reserved)

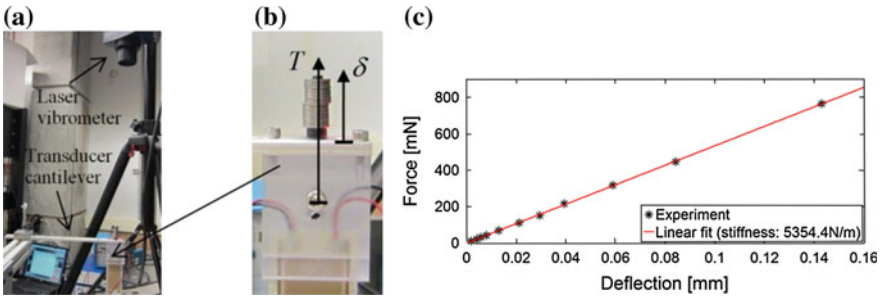

Fig. 10 **a** Setup used for the thrust-displacement calibration experiment with the MFC bimorph, its clamp, and the transducer cantilever; **b** close-up view showing the point of applied loads at the center of MFC bimorph and the deflection measurement point; **c** linear calibration curve with the calculated linear stiffness (T/δ) value (© IOP Publishing. Reproduced with permission. All rights reserved)

This laser vibrometer employed for measuring the head displacement corresponds to Laser (2) in the underwater experiments (Fig. 9a). The purpose of the in-air setup shown in Fig. 10a is to relate the thrust caused by actuation in the underwater experiments to the deflection of the aluminum transducer cantilever as detailed in Sect. 2 (however, this is a separate setup and is not identical to that in Fig. 2). It is assumed that the mean thrust resultant (T) of the bimorph propulsor (in the underwater experiments) acts through the center of its head, causing the deflection of δ at the location of the reflector for Laser (2) in the underwater arrangement given by Fig. 9a. Different values of small masses are gradually located at the center of the top surface to emulate the mean thrust (Fig. 10b). The vertically pointing laser measures the resulting deflection at the reflector, which is employed to obtain the thrust-displacement calibration line shown in Fig. 10c.

5 Experiments and Model Validation

5.1 In-Air Tip Velocity FRF and Parameter Identification

Low-voltage harmonic input is applied to the MFC bimorph for the frequency range of 5–70 Hz with an increment of 0.05 Hz. Figure 11a exhibits the experimentally measured tip velocity-to-actuation voltage FRF and the model prediction using Eq. (13) for the linear actuation regime of the bimorph. The fundamental in-air resonance frequency is 35.5 Hz. The in-air damping ratio (attributed mostly to structural losses for small oscillations) is identified as $\zeta_s = 0.02$ while the identified electromechanical coupling in the physical coordinates [see Eq. (1)] is $\vartheta = 23.03\,\mu\text{Nm/V}$. The modal electromechanical coupling that depends on the in-air eigenfunction due to Eq. (10) is $\theta = 8.878 \times 10^{-3}$ N/(Vkg$^{-1/2}$).

5.2 Underwater Tip Velocity FRF

The MFC bimorph is submerged in water (as depicted in Fig. 9) along with its clamp and aluminum fixture used in thrust calibration (Fig. 10). Low-voltage harmonic actuation is applied to the MFC bimorph for the frequency range of 2–15 Hz with an increment of 0.05 Hz. The fundamental underwater resonance frequency of linear vibrations is measured as 8.7 Hz. According to Eq. (16), the total underwater damping ratio is due to the structural and hydrodynamic damping effects. Equation (15) yields $\zeta_h = 0.0119$ and $Re \cong 19{,}430$, and eventually, from Eq. (16), one obtains $\zeta_w = 0.0319$. The electromechanical coupling in the physical coordinates is the same as the one obtained from in-air vibration test ($\vartheta = 23.03\,\mu\text{Nm/V}$) while the modal electromechanical coupling becomes $\theta = 2.325 \times 10^{-3}$ N/(Vkg$^{-1/2}$) due to Eq. (10) in which the eigenfunction is normalized according to Eq. (19) by using the underwater mass per length given by Eq. (17). Therefore, one can predict the underwater tip velocity FRF using Eq. (21) as shown in Fig. 11b.

The agreement between the experimental measurement and theoretical prediction is reasonable in the linear actuation regime of the bimorph. Equation (20) predicts the underwater resonance frequency as 8.8 Hz with an error of 1.1 % relative to the experimental value (8.7 Hz). Both the total underwater damping and natural frequency are predicted in terms of the in-air dynamics and fluid properties with good accuracy. Expectedly, the linear model predictions would fail under high actuation voltage levels due to geometric and electroelastic nonlinearities [58–60]. Nonlinear modeling of MFC dynamics under high-voltage actuation and incorporation of nonlinear hydrodynamic effects [66] in such a nonlinear model are of interest for future work.

5.3 Mean Thrust and Tip Velocity Correlation for Different Actuation Voltage Levels

The frequency range covered in the underwater thrust measurements is 0.5–15 Hz with a fine increment of 0.25 Hz in the 6–8 Hz range (resonance region) and a

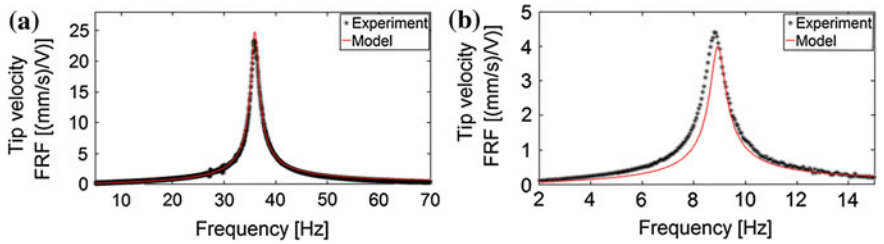

Fig. 11 Measured and calculated **a** in-air and **b** underwater tip velocity-to-actuation voltage FRFs of the MFC bimorph in its linear actuation regime (© IOP Publishing. Reproduced with permission. All rights reserved)

relatively coarse increment of 0.5 Hz outside the resonance region. Three time-domain head displacement measurements are taken at each frequency (preactuation, actuation, and post-actuation as detailed in Sect. 2.2) while the tip velocity in the transverse direction is measured simultaneously. The reference point is calculated as the average of the preactuation and post-actuation values. Based on the previously discussed calibration, the mean thrust is a linear function of the mean displacement of the aluminum cantilever. This mean displacement is the difference between the mean values of the *actuation* displacement and the *reference* point. From this mean displacement, the mean thrust is extracted using the linear calibration curve in Fig. 9c.

The experimental tip velocity and mean thrust measurements for the peak-to-peak actuation voltage levels of 200, 400, 600, and 800 V are shown in Fig. 12a, b, respectively. Clearly, there is a direct correlation between these two independent measurements since the thrust level increases with increasing tip velocity. It should be noted that these high actuation voltage levels fall into the nonlinear regime due to the electroelastic, geometric, and dissipative nonlinear effects. The softening nonlinearity (resulting in the shifting of the resonance frequency to the left) with increased actuation input is a typical behavior of piezoelectric cantilevers under high-voltage actuation [59].

Using Eq. (24) resulting from Lighthill's theory for the quiescent water condition, one can estimate the thrust curves in terms of the tip velocity and the virtual mass. These predictions are shown in Fig. 13a–d for four different actuation voltage levels. Note that, particularly in Fig. 13a (which is the lowest voltage case among these four measurement sets), the frequencies away from the resonance region are

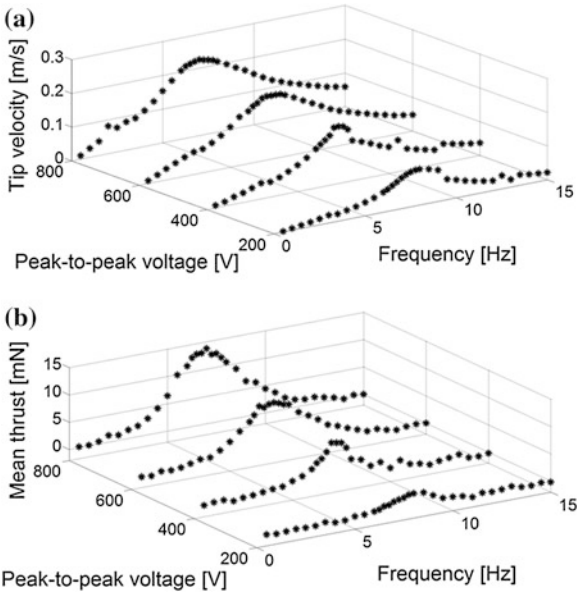

Fig. 12 Experimental **a** tip velocity and **b** mean thrust curves for four different peak-to-peak voltage levels: 200, 400, 600, and 800 V (© IOP Publishing. Reproduced with permission. All rights reserved)

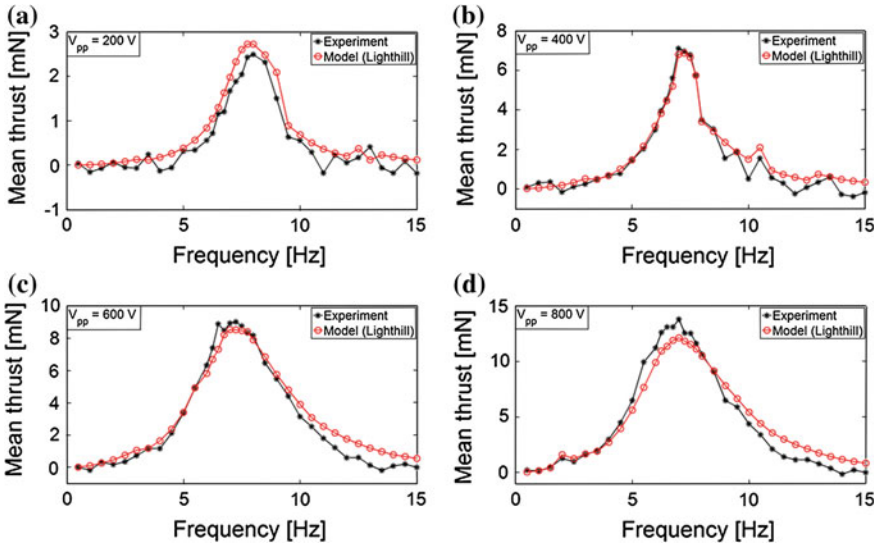

Fig. 13 Measured and predicted thrust curves for the peak-to-peak voltage inputs of **a** 200 V, **b** 400 V, **c** 600 V, and **d** 800 V (© IOP Publishing. Reproduced with permission. All rights reserved)

prone to noise effects in the measurements due to low thrust resultant (caused by low displacement). Based on Fig. 13a–d, it can be concluded that the reduced form of Lighthill's theory [69–71] for quiescent water can predict the mean thrust in terms of the tip velocity with good accuracy. One should recall that Figs. 12 and 13 are electroelastically nonlinear, and therefore the linear derivations given in this chapter do not intent to predict these dynamics quantitatively. However, Lighthill's formula reduced for quiescent water in Sect. 3.3 does correlate the tip velocity-to-mean thrust with reasonable accuracy in Fig. 13 as a first approximation.

5.4 Identification of the Thrust Coefficient

In this section, the hydrodynamic thrust coefficient of the propulsor is extracted based on the mean thrust and transverse tip velocity of the piezoelectric propulsor. First we define the modified Reynolds number as

$$Re_L = \frac{\omega \delta L}{\upsilon}, \tag{25}$$

where $\delta = |w(L,t)|$ is the tip displacement amplitude at frequency ω while υ is the kinematic viscosity of water ($\upsilon = \mu/\rho_w$). Note that the modified Reynolds number introduced at this point uses the underwater vibration response as the geometric scale (rather than the width).

The thrust coefficient C_τ is defined as [73]

$$C_\tau = \frac{\tau}{\frac{1}{2}\rho_w \omega^2 \delta^2 L}, \tag{26}$$

where τ is the thrust per unit width ($\tau = T/b$) and we note from Eqs. (25) and (26) that $\tau \propto Re_L^2$.

Substituting Eq. (24) into Eq. (26) gives

$$C_\tau = \frac{\frac{\pi\rho_w b}{8}\overline{\left(\frac{\partial w(L,t)}{\partial t}\right)^2}}{\frac{1}{2}\rho_w \omega^2 \delta^2 L} = \frac{\frac{\pi\rho_w b}{8}\frac{\omega^2\delta^2}{2}}{\frac{1}{2}\rho_w \omega^2 \delta^2 L} = \frac{\pi b}{8L} \cong 0.1524 \tag{27}$$

Another manipulation of Eqs. (25) and (26) provides the variation of the mean thrust with modified Reynolds number as

$$T = \frac{\pi \rho_w b^2 \upsilon^2}{16 L^2} Re_L^2 \cong 3.322 \times 10^{-11} Re_L^2 \quad \text{[in Newtons]} \tag{28}$$

Figure 14 displays the variation of the mean thrust with modified Reynolds number based on the experimental thrust measurements at different actuation voltage levels and frequencies along with the prediction of Eq. (28) in log–log scale. The proportionality between mean thrust T and Re_L^2 is observed in the experimental data and is well predicted by the modeling approach based on Lighthill's theory.

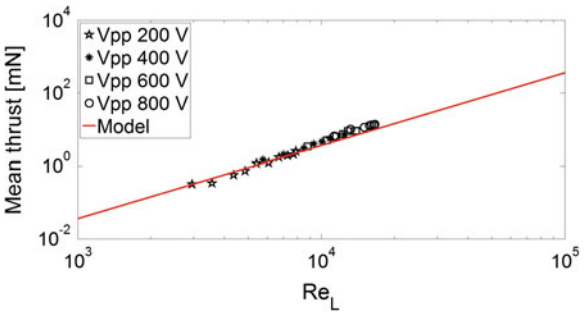

Fig. 14 Experimental and theoretical mean thrust versus the modified Reynolds number. The experimental data belongs to four different actuation voltage levels and different frequencies around the fundamental resonance (© IOP Publishing. Reproduced with permission. All rights reserved)

6 Prototype for Untethered Locomotion

6.1 Electronic Architecture for Untethered Swimming

Despite the advantages of MFCs due to large dynamic actuation stresses, structural flexibility, silent operation, and wide frequency range of effective performance, the requirement of high-voltage input limits its application in free (untethered) locomotion for robotic fish development. In this section, a PCB high-voltage amplifier is implemented along with a microcontroller to overcome this issue in free locomotion. To our knowledge, this section presents the first untethered piezoelectric robotic fish since the configurations in previous efforts [52–55] were actuated through external power through tethers.

A separate bimorph propulsor is fabricated for the free locomotion experiments. An embedded power and actuation system is designed for this prototype, which can generate high-input voltage for the MFC bimorph propulsor. As shown in Fig. 15a, this system consists of two 9 V batteries, a microcontroller (ATmega 128), a wireless device [XBee 1mW Wire Antenna—Series 1 (802.15.4)], and a PCB amplifier (AMD2012-CE3) specially designed for the MFC actuator [51]. In order to obtain smooth sinusoidal voltage for the MFC bimorph, a low-pass filter is added

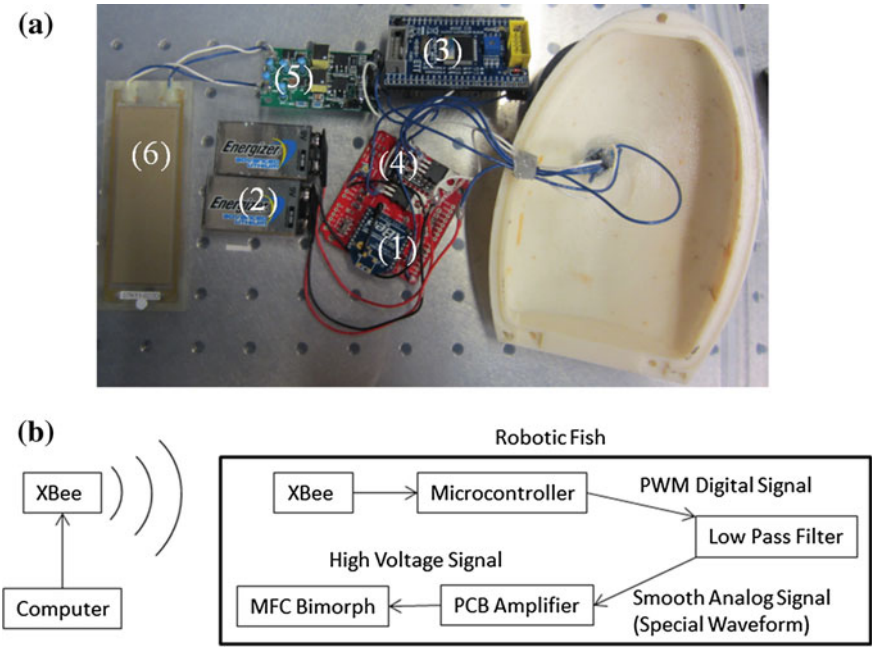

Fig. 15 **a** Components for the untethered piezoelectric robotic fish system: *(1)* XBee radio; *(2)* 9 V batteries; *(3)* microcontroller; *(4)* low pass filter and voltage regulators; *(5)* voltage amplifier; *(6)* MFC bimorph; and **b** electronic schematic of the robotic fish system (© IOP Publishing. Reproduced with permission. All rights reserved)

to filter out the high-frequency noise from the pulse width modulation (PWM) signals. The detailed schematic of the actuation system is shown in Fig. 15b.

6.2 Power Consumption Analysis

In order to enable untethered locomotion of the MFC-based robotic fish, a portable power system has to be designed to generate the high voltage for MFC bimorph actuation. The general maximum output voltage level for the microcontroller is around 5 volts, which is much lower than the requirements for MFC actuation. A specifically designed PCB amplifier (AMD2012-CE3) [51] is utilized in the power system, which is able to generate high voltage from −500 to 1500 V according to the control input signal from 0 to 5 V. This PCB amplifier requires only 12 V input voltage supply. Therefore, one can build the mobile power system by simply using two 9 V batteries, the microcontroller, the PCB amplifier, and the corresponding voltage regulators, as shown in Fig. 15a. These two 9 V batteries can support the continuous operation of the system for almost 30 min. The power consumption of the overall electronic system is around 3–5 W.

The current amplitude and average power plots for MFC bimorph vibration under different frequencies and actuation voltages are shown in Fig. 16. Figure 16b shows that the average power input to the MFC bimorph around its fundamental mode is less than 1 W (for the sinusoidal peak-to-peak voltage of 800 V). It should be noted that the results in Fig. 16b is an overestimation as far as the truly consumed (real) power is concerned since these modulus curves include not only resistive but also reactive power. The overall power consumption of the robotic fish can therefore be further reduced by optimizing the actuation circuit design.

6.3 Microcontroller, PCB Voltage Amplifier, and Wireless Control

In order to provide sinusoidal high voltage for the MFC bimorph, the microcontroller is programmed to generate a special waveform by PWM. Specifically, 0 V

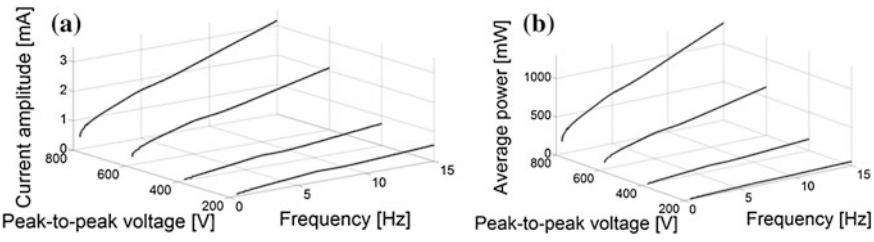

Fig. 16 Experimental **a** current amplitude and **b** average power curves of the MFC bimorph under four different peak-to-peak voltage levels: 200, 400, 600, and 800 V (© IOP Publishing. Reproduced with permission. All rights reserved)

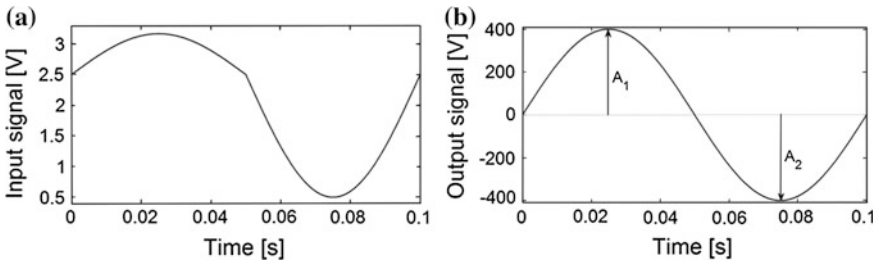

Fig. 17 **a** Input and **b** output signals of the PCB amplifier to generate a sinusoidal peak-to-peak actuation voltage of 800 V at 10 Hz. The microcontroller can provide signal inputs to PCB amplifier to create oscillatory actuation voltage signals with $A_1 \neq A_2$ for turning motion (© IOP Publishing. Reproduced with permission. All rights reserved)

input signal generates −500 V output; 2.5 V input signal generates 0 V output; 5 V input signal generates 1500 V output. These values are the voltage limits of MFCs without depolarization [51]. An example is given in Fig. 17 for the case of generating a sinusoidal peak-to-peak voltage of 800 V at 10 Hz using the PCB amplifier. The microcontroller is able to generate various waveforms by its PWM function and the power system can provide the high-voltage sinusoidal output (up to 2000 V peak-to-peak) for the MFC bimorph propulsor. The frequency, mean voltage, and amplitudes of the PCB amplifier output signal can be controlled by adjusting the rate and duty cycle of the PWM signals. The swimming speed is easily controlled through PCB amplifier output signal frequencies and amplitudes. In addition, turning speed and direction are controlled by setting different values for the amplitudes A_1 and A_2 shown in Fig. 17b. Wireless control is performed through serial communication. Commands are sent by a laptop computer through a USB connected XBee Explorer. An XBee module inside the robotic fish body receives the commands and transfers them to the microcontroller, which can change the PWM waveform. Therefore, wireless communication controls the swimming speed of the robotic fish by setting the rate and duty cycle of the PWM, which affect the vibration frequency and amplitude of the MFC propulsor. The Xbee signal would penetrate the water just a few centimeters so the robotic fish is tested close to surface. The wireless communication is used for testing the change of speed and direction during swimming.

6.4 Fabricated Prototype and Free Locomotion Tests

A picture of the robotic fish prototype is shown in Fig. 18. The fish body is designed to provide a waterproof enclosure for the electronics components and is realized using a Fused Deposition Modeling (FDM) machine. This creates an Acrylonitrile Butadiene Styrene (ABS) plastic shell, that when printed is buoyant in water. An O-ring was integrated into the rim to ensure the interior of the fish stayed

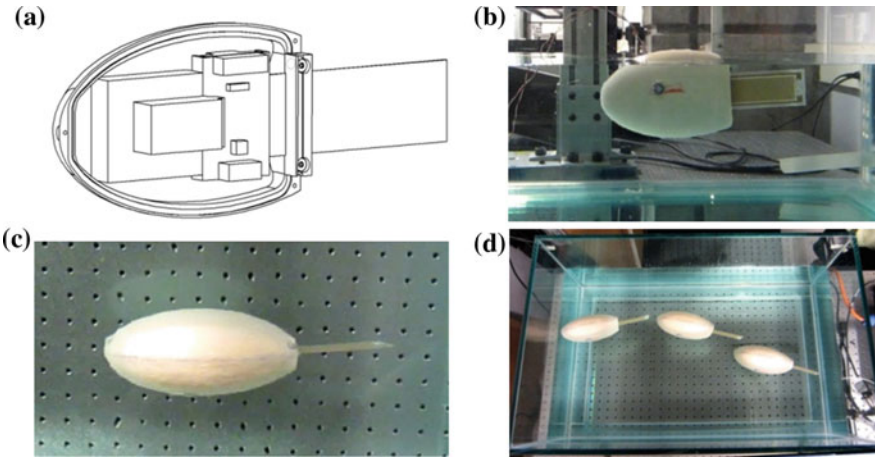

Fig. 18 Untethered robotic fish prototype for free locomotion in **a** modeled view; **b** side-view; **c** top view; and **d** combined motion capture involving turning motion. Swimming speed under peak-to-peak actuation voltage of 1000 V at 5 Hz is approximately 7.5 cm/s (© IOP Publishing. Reproduced with permission. All rights reserved)

dry in order to protect the electronics. This prototype is intended merely for proof of concept, as the nonoptimized volume (and hence buoyant force) requires a significant amount of counterweight.

The swimming speed for a peak-to-peak actuation voltage of 1000 V at 5 Hz is measured as 7.5 cm/s (measured by video recording).[1] This is equivalent to almost 0.3 body length/s and it compares favorably with several smart actuator-based aquatic robots reported in the literature (including tethered ones) [3] even though the present prototype excludes the additional passive caudal fin extension and volumetric optimization. The passive caudal fin extension is known to improve not only the thrust amplitude but also the bandwidth of effective excitation frequencies (see Figs. 5 and 6). Further improvements can be made by increasing the actuation voltage to a larger level with a DC offset (since MFC laminates have asymmetric voltage limits: −500 to 1500 V).

In general, motor-based robotic fish has larger speed per body length than smart material-based counterparts, whereas the latter offers ease of fabrication and geometric scalability. According to the comparative study by Cen and Erturk [56], the preliminary MFC robotic fish design presented in this work is near the intersection of smart material-based and motor-based robotic fish. Therefore, MFC-based robotic fish provides geometric scalability (as compared to motor-based robotic fish) and high performance swimming (as compared to IPMC-based robotic fish).

[1]Note that the boundary conditions in free (unconstrained) locomotion are no longer clamped-free due to the hardware attachment at the head with finite translational and rotary inertia (which can be accounted for in structural dynamic modeling). Therefore, the resonance frequencies of Fig. 9 (clamped-free) and Fig. 18 (free-free with hardware) cases are different.

7 Conclusions

Bio-inspired aquatic robotics using MFC piezoelectric bimorphs is investigated for fish-like locomotion. First, the effect of a passive substrate fin extension on the thrust frequency response of MFC bimorphs in quiescent water is presented along with measurement procedures. Specifically it is shown that broadband thrust generation can be achieved in the presence of a passive substrate extension. In-air and underwater dynamics of an MFC bimorph cantilever are then modeled for small amplitude bending vibrations under piezoelectric actuation. Underwater dynamics of the bimorph propulsor is coupled with Lighthill's elongated-body theory to predict the thrust output in quiescent water. In-air and underwater experiments are conducted for model validation and for the characterization of a bimorph propulsor. Simplified hydrodynamics is assumed to estimate the underwater electrohydroelastic behavior. For future work, nonlinear electrohydroelastic modeling (combining nonlinear electroelastic dynamics [58–60] with nonlinear hydrodynamic effects [66]) is required to predict the dynamics of the propulsor for large oscillations, comparable length-to-width aspect ratios, and under high electric field levels.

The underwater experiments resulted in mean thrust levels as high as 14 mN around 7 Hz for the peak-to-peak actuation voltage of 800 V using a 90 mm × 35 mm × 0.67 mm cantilever in the absence of a passive fin extension (note that the MFCs can perform without depolarization up to peak-to-peak actuation voltage of 2000 V). In the presence of a passive caudal fin extension, not only the frequency bandwidth but also the thrust levels can be enhanced substantially. The passive caudal fin brings the second vibration mode close to the first one and makes the smart fish a wideband thrust generator. The effect of actuation voltage on the thrust output is also investigated for the fish configuration with a passive caudal fin. For the highest actuation voltage level, mean thrust values of more than 30 mN are obtained in the frequency range of 4–17 Hz (with the peak values of 40 and 50 mN at the first two resonance frequencies, respectively). Overall, fish-like propulsors made from MFCs can successfully imitate thrust levels of biological fish (see Lauder and Drucker [74] for typical values).

An untethered robotic fish prototype that incorporates a microcontroller and a printed-circuit-board amplifier is developed and tested in free locomotion. A swimming speed of 0.3 body length/s (7.5 cm/s swimming speed for 24.3 cm body length) is achieved for a nonoptimized main body–propulsor combination. This swimming speed can be improved substantially by increasing the actuation voltage, optimizing the volume, and using a passive fin extension. According to normalized swimming speed vs. body length comparison by Cen and Erturk [56] with the literature of untethered robotic fish, the MFC-based robotic fish provides geometric scalability and high performance swimming, located at the intersection of smart material-based and motor-based swimmers with these favorable characteristics.

Acknowledgements The author acknowledges contributions of his previous undergraduate visiting researcher Mr. Ghislain Delporte (formerly at Virginia Tech) and of his previous master's student Mr. Lejun Cen (at Georgia Tech) to the original work that is reviewed in this chapter. The author also acknowledges support from the NSF Grant CMMI-1254262 for the ongoing research efforts.

References

1. Bandyopadhyay PR (2005) Trends in biorobotic autonomous undersea vehicles. IEEE J Ocean Eng 30(1):109–139
2. Roper D et al (2011) A review of developments towards biologically inspired propulsion systems for autonomous underwater vehicles. Proc Inst Mech Eng [M] J Eng Marit Environ 225(2):77–96
3. Chu WS et al (2012) Review of biomimetic underwater robots using smart actuators. Int J Precis Eng Manufact 13(7):1281–1292
4. Barrett DS (1994) The design of a flexible hull undersea vehicle propelled by an oscillator foil. MS thesis, Department of Ocean Engineering, Massachusetts Institute of Technology, Boston, 177 pp
5. Barrett DS (1996) propulsive efficiency of a flexible hull underwater vehicle. PhD thesis, Department of Ocean Engineering, Massachusetts Institute of Technology, Boston, 215 pp
6. Anderson JM, Chhabra V (2002) Maneuvering and stability performance of a robotic tuna. Integr Comp Biol 42(1):118–126
7. Low K, Willy A (2006) Biomimetic motion planning of an undulating robotic fish fin. J Vib Control 12(12):1337–1359
8. Valdivia y Alvarado P (2007) design of biomimetic compliant devices for locomotion in liquid environments. PhD thesis, Department of Ocean Engineering, Massachusetts Institute of Technology, Boston, 164 pp
9. Crespi A et al (2008) Controlling swimming and crawling in a fish robot using a central pattern generator. Auton Robot 25(1):3–13
10. Liu F, Lee KM, Yang CJ (2012) Hydrodynamics of an undulating fin for a wave-like locomotion system design. IEEE/ASME Trans Mech 17(3):554–562
11. Zhou C, Low K (2012) Low, design and locomotion control of a biomimetic underwater vehicle with fin propulsion. IEEE/ASME Trans Mech 17(1):25–35
12. Wen L et al (2012) Quantitative thrust efficiency of a self-propulsive robotic fish: experimental method and hydrodynamic investigation. IEEE/ASME Trans Mechatron 18(3):1027–1038
13. Serchi FG, Arienti A, Laschi C (2012) Biomimetic vortex propulsion: toward the new paradigm of soft unmanned underwater vehicles. IEEE/ASME Trans Mechatron 18(2):484–493
14. Shahinpoor M (1992) Conceptual design, kinematics and dynamics of swimming robotic structures using ionic polymeric get muscles. Smart Materials and Structures 1:91–95
15. Mojarrad M, Shahinpoor M (1996) Noiseless propulsion for swimming robotic structures using polyelectrolyte ion-exchange membrane. Smart Mater Technol Biomim Smart Struct Mater 1996(2716):183–192
16. Laurent G, Piat E (2001) Efficiency of swimming microrobots using ionic polymer metal composite actuators. In: Proceedings IEEE international conference on robotics and automation, vol I–IV, pp 3914–3919
17. Kim KJ (2003) Fabrication and development of electroactive ionic polymer-metal composites and their applications as smart materials. THERMEC'2003, pts 1-5, vol 426–424, pp 2249–2254
18. Kim B et al (2005) A biomimetic undulatory tadpole robot using ionic polymer-metal composite actuators. Smart Mater Struct 14(6):1579–1585

19. Chung CK et al (2005) A novel fabrication of ionic polymer-metal composites (IPMC) actuator with silver nano-powders. Transducers 05, digest of technical papers, vol 1–2, pp 217–220
20. Guo SX et al (2006) Underwater swimming micro robot using IPMC actuator. In: Proceeding of the 2006 IEEE international conference on mechatronics and automation, IEEE ICMA 2006, vol 1–3, pp 249–254
21. Chung CK et al (2006) A novel fabrication of ionic polymer-metal composites (IPMC) actuator with silver nano-powders. Sens Actuators B 117(2):367–375
22. Tan XB et al (2006) An autonomous robotic fish for mobile sensing. In: IEEE/RSJ 2006 international conference on intelligent robots and systems, vol 1–12, pp 5424–5429
23. Brunetto P et al (2008) A model of ionic polymer-metal composite actuators in underwater operations. Smart Mater Struct 17(2):12
24. Mbemmo E et al (2008) Modeling of biomimetic robotic fish propelled by an ionic polymer-metal composite actuator. In: IEEE international conference on robotics and automation, vol 1–9, pp 689–694
25. Jeon JH, Yeorn SW, Oh IK (2008) Fabrication and actuation of ionic polymer metal composites patterned by combining electroplating with electroless plating. Compos A Appl Sci Manufact 39(4):588–596
26. De Witt BJ, Hugo RJ (2009) A preliminary study of the transition of an in-line pipe vortex to slug flow using particle image velocimetry. In: Proceedings of the ASME fluids engineering division summer conference-2008, vol 1, pt a and b, pp 637–646
27. Chen Z, Shatara S, Tan XB (2010) Modeling of biomimetic robotic fish propelled by an ionic polymer-metal composite caudal fin. IEEE-ASME Trans Mechatron 15(3):448–459
28. Aureli M, Kopman V, Porfiri M (2010) Free-locomotion of underwater vehicles actuated by ionic polymer metal composites. IEEE-ASME Trans Mechatron 15(4):603–614
29. Takagi K et al (2006) Development of a Rajiform swimming robot using ionic polymer artificial muscles. In: IEEE/RSJ international conference on intelligent robots and systems, vol 1–12, pp 1861–1866
30. Chen Z, Um TI, Zhu J (2011) Bio-inspired robotic cownose ray propelled by electroactive polymer pectoral fin. In: ASME 2011 international mechanical engineering congress and exposition
31. Chen Z, Um TI, Bart-Smith H (2011) Ionic polymer-metal composite enabled robotic manta ray. In: Proceedings of SPIE 7976:797637
32. Shinjo N, Swain GW (2004) Use of a shape memory alloy for the design of an oscillatory propulsion system. IEEE J Ocean Eng 29(3):750–755
33. Wang ZL et al (2008) A micro-robot fish with embedded SMA wire actuated flexible biomimetic fin. Sens Actuators A 144(2):354–360
34. Wang Z et al (2008) Embedded SMA wire actuated biomimetic fin: a module for biomimetic underwater propulsion. Smart Mater Struct 17:025039
35. Cho KJ et al (2008) Design, fabrication and analysis of a body-caudal fin propulsion system for a microrobotic fish. In: IEEE international conference on robotics and automation, vol 1–9, pp 706–711
36. Rossi C et al (2011) Bending continuous structures with SMAS: a novel robotic fish design. Bioinspir Biomim 6:045005
37. Rossi C et al (2011) A motor-less and gear-less bio-mimetic robotic fish design. IEEE International Conference on Robotics and Automation, pp 3646–3651
38. Zhang YS, Liu GJ (2005) Design, analysis and experiments of a wireless swimming micro robot. In: IEEE international conference on mechatronics and automations, vol 1–4, pp 946–951
39. Zhang YS, Liu GJ (2005) Wireless micro biomimetic swimming robot based on giant magnetostrictive films. IEEE Int Conf Rob Biomim 2006:195–200
40. Zhang YS, Liu GJ (2009) Wireless swimming microrobot: design, analysis, and experiments. J Dyn Syst Meas Control Trans ASME 131(1):014502

41. Zhang Z (2007) Design and control of a fish-like robot using an electrostatic motor. In: IEEE Proceedings of ICRA, Rome
42. Zhang Z, Philen M, Neu W (2010) A biologically inspired artificial fish using flexible matrix composite actuators: analysis and experiment. Smart Mater Struct 19:094017
43. Philen M, New W (2011) Hydrodynamic analysis, performance assessment, and actuator design of a flexible tail propulsor in an artificial alligator. Smart Mater Struct 20:094015
44. Uchino K (2008) Piezoelectric actuators 2006—expansion from IT/Robotics to ecological/energy applications. J Electroceram 20(3–4):301–311
45. Cook-Chennault KA, Thambi N, Sastry AM (2008) Powering MEMS portable devices—a review of non-regenerative and regenerative power supply systems with special emphasis on piezoelectric energy harvesting systems. Smart Mater Struct 17(4):043001
46. Erturk A, Delporte D (2011) Underwater thrust and power generation using flexible piezoelectric composites: an experimental investigation toward self-powered swimmer-sensor platforms. Smart Mater Struct 20:125013
47. Trolier-Mckinstry S, Muralt P (2004) Thin film piezoelectrics for MEMS. J Electroceram 12 (1–2):7–17
48. Wilkie WK et al (2000) Low-cost piezocomposite actuator for structural control applications. In: Proceedings of SPIE, 3991:323
49. High JW, Wilkie WK (2003) Method of fabricating NASA-standard macro-fiber composite piezoelectric actuators, National Aeronautics and Space Administration, Langley Research Center
50. Bryant RG (2007) Overview of NASA langley's piezoelectric ceramic packaging technology and applications, National Aeronautics and Space Administration, Langley Research Center
51. Smart Material Corp. http://www.smart-material.com
52. Fukuda T et al (1995) Steering mechanism and swimming experiment of micro mobile robot in water. In: IEEE proceedings on micro electro mechanical systems, pp 300–305
53. Heo S et al (2007) Effect of an artificial caudal fin on the performance of a biomimetic fish robot propelled by piezoelectric actuators. J Bionic Eng 4(3):151–158
54. Wiguna T et al (2009) Design and experimental parameteric study of a fish robot actuated by piezoelectric actuators. J Intell Mater Syst Struct 20(6):751–758
55. Ming AG et al (2009) Development of underwater robots using piezoelectric fiber composite. In: IEEE international conference on robotics and automation ICRA, vol 1–7, pp 3435–3440
56. Cen L, Erturk A (2013) Bio-inspired aquatic robotics by untethered piezohydroelastic actuation. Bioinspir Biomim 8:016006
57. Meirovitch L (2001) Fundamentals of vibrations, vol XVIII. Mcgraw-hill, Boston, p 806
58. Wolf K, Gottlieb O (2002) Nonlinear dynamics of a noncontacting atomic force microscope cantilever actuated by a piezoelectric layer. J Appl Phys 91(7):4701–4709
59. Usher T, Sim A (2005) Nonlinear dynamics of piezoelectric high displacement actuators in cantilever mode. J Appl Phys 98(6):064102
60. Stanton SC et al (2012) Nonlinear nonconservative behavior and modeling of piezoelectric energy harvesters including proof mass effects. J Intell Mater Syst Struct 23(2):183–199
61. Sader JE (1998) Frequency response of cantilever beams immersed in viscous fluids with applications to the atomic force microscope. J Appl Phys 84(1):64–76
62. Van Eysden CA, Sader JE (2007) Frequency response of cantilever beams immersed in viscous fluids with applications to the atomic force microscope: arbitrary mode order. J Appl Phys 101(4):044908
63. Chon JWM, Mulvaney P, Sader JE (2000) Experimental validation of theoretical models for the frequency response of atomic force microscope cantilever beams immersed in fluids. J Appl Phys 87(8):3978–3988
64. Aureli M, Porfiri M (2010) Low frequency and large amplitude oscillations of cantilevers in viscous fluids. Appl Phys Lett 96(16):164102
65. Maali A et al (2005) Hydrodynamics of oscillating atomic force microscopy cantilevers in viscous fluids. J Appl Phys 97(7):074907

66. Aureli M, Basaran ME, Porfiri M (2012) Nonlinear finite amplitude vibrations of sharp-edged beams in viscous fluids. J Sound Vib 331(7):1624–1654
67. Chu W (1963) Technical report no. 2. DTMB, contract NObs-86396 (X), Southwest Research Institute, San Antonio, Texas
68. Lighthill MJ (1960) Note on the swimming of slender fish. J Fluid Mech 9(2):305–317
69. Lighthill MJ (1969) Hydromechanics of aquatic animal propulsion. Annu Rev Fluid Mech 1:413–446
70. Lighthill MJ (1970) Aquatic animal propulsion of high hydromechanical efficiency. J Fluid Mech 44:265–301
71. Lighthill MJ (1971) Large-amplitude elongated-body theory of fish locomotion. Proc R Soc Lond B Biol Sci 179(1055):125–138
72. Anton SR, Erturk A, Inman DJ (2010) Multifunctional self-charging structures using piezoceramics and thin-film batteries. Smart Mater Struct 19(11):115021
73. Abdelnour K et al (2009) Hydrodynamics of underwater propulsors based on ionic polymer-metal composites: a numerical study. Smart Mater Struct 18(8):085006
74. Lauder GV, Drucker EG (2002) Forces, fishes, and fluids: hydrodynamic mechanisms of aquatic locomotion. News Physiol Sci 17:235–240